Toward the modeling of static electric field effects in rhodopsin photophysics using QM/MM calculations

Isabel Eder, Miquel Huix-Rotllant, Nicolas Ferré

Towards the modeling of static electric field effects in rhodopsin photophysics using QM/MM calculations

Isabel Eder[1], Miquel Huix-Rotllant[1], Nicolas Ferré[1*]

[1*]Aix Marseille Univ, CNRS, ICR, Marseille, 13013, France.

*Corresponding author(s). E-mail(s): nicolas.ferre@univ-amu.fr;
Contributing authors: isabel.eder@univ-amu.fr;
miquel.huix-rotllant@cnrs.fr;

Abstract

A transmembrane voltage, arising from ion imbalance between the extracellular and cytoplasmic sides of a cell, can influence the biological function of transmembrane proteins. At the atomistic scale, transmembrane voltage can be modeled thanks to the application of an external electric field. Here, we introduce a new QM/MM model capable of efficiently describing the interaction of QM and MM atoms with a static electric field (SEF) thanks to ElectroStatic Potential Fitted (ESPF) operators. A simple decomposition of the full interaction energy is proposed in terms of electrostatic QM/MM interactions and interactions of QM and MM multipoles with the SEF. Having validated the method and tested its limitations in the case of a short protonated Schiff base model, it is applied to the case of the Gloeobacter Rhodopsin, a transmembrane photoactive protein with potential applications in optogenetics. In particular, we evidence that a weak electric field only perturb the local electric field, due to the protein amino-acids.

Keywords: QM/MM, rhodopsin, photoisomerisation, static electric field

1 Introduction

Transmembrane proteins experience a voltage difference between their inner (intracellular) and outer (cytoplasmic) sides, due to local ion charge imbalance. The resulting electric field, typically on the order of 0.1 to a few MV cm^{-1}[1], can have important impact on protein functions like ion transport [2] or to applications like voltage sensing

in optogenetics[3]. For this latter application, light-driven ion pumps or light-gated ion channels are necessary to hyper- and depolarize neuronal cells. Both functions can be found in rhodopsins, a class of transmembrane proteins containing a protonated Schiff base called retinal as chromophore. While the primary event in virtually all rhodopsins is the light-activated retinal isomerization in its first excited state, the fluorescence (a minor deactivation channel) of microbial rhodopsin engineered mutants can be used for monitoring the membrane voltage [4], with important application in optogenetics to control cell signaling[5]. Interestingly, in the particular case of the sodium pump *Krokinobacter eikastus* rhodopsin 2, it has been recently shown that a sodium cation remains in close contact with the chromophore within one millisecond [6]. This finding suggests a large modification of the electric field experienced by the chromophore, whose electronic properties are altered, including the influence on the isomerization of *all-trans* to *13-cis retinal*.

The atomistic modeling of electric fields effects on transmembrane protein activities is usually based on two complementary approaches: (i) an explicit charge imbalance is introduced in the model[7], or (ii) an external static electric field (SEF) is imposed [8]. In practice, both approaches are often shown to produce equivalent results with respect to the transmembrane potential, field intensity and charge density.[9, 10]

In the charge imbalance model, the electric field is created by introducing two different ion concentrations on each side of the membrane. This approach requires either a second membrane or water/air interfaces to accurately define the electrolyte concentration imbalance when periodic boundary conditions are employed.[7, 9] On the one hand, models with a double membrane have a significant increase in computational cost due to the larger system size. On the other hand, sandwiching the membrane between two air/water interfaces keeps a more trackable system size, the water layers being about 30 Å thick. Since the number of ions is adjusted by the user, it is also challenging to fine-tune the transmembrane voltage to a specific value.[9]

Alternatively, a computationally more efficient way of introducing the transmembrane voltage is to add an external SEF acting on all atoms in the system instead of an atomistic charge imbalance. This is based on Poisson-Boltzmann theory, stating that the membrane potential becomes linear in periodic boundary conditions. Its force is equivalent to the one of a constant electric field, only depending on the electric field strength and the length of the simulation box.[8] Advantageously, this model simplifies the complex system of ion pumps and channels. It can also be applied to study the effect of ultrashort (ns time scale) electric field pulses, with the possible drawback of generating nonphysical distributions of ions, because of the small size of the system.[7]

The main goal of the present study is to develop an efficient computational framework to model the effect of transmembrane voltage effects on the photophysical properties of transmembrane proteins via SEF. In particular, we focus on the effect of a SEF on the absorption spectrum of a simple model, ie. the *Gloeobacter* rhodopsin (GR) in gas phase, a microbial proton pump[11] for which fluorescent mutants have already been proposed.[12, 13] Regarding its retinal chromophore, pioneer work by Garavelli and coworkers[14] reported the effect of SEF on the gas phase *all-trans* retinal excited states. They found that, depending on the orientation of the electric field along the conjugated π-system, its S_1 state is either destabilized and mixes with higher

excited states or it is stabilized, eventually resulting in an avoided crossing with its ground state S_0. These trends are rationalized on the basis of the charge transfer character of S_1, highly sensitive to the SEF. Nevertheless, in a rhodopsin the retinal chromophore also experiences a local electric field originating from the opsin charge distribution; opsin refering to the protein structure without the chromophore. This local electric field competes with the applied SEF and could therefore lead to amplified or quenching effects.

In the next section, we succinctly recall the modifications in the molecular electronic Hamiltonian to account for the interaction with an external SEF, and subsequently formulate the external SEF interaction in the framework of a hybrid quantum mechanics/molecular mechanics (QM/MM) approach, [15–17] in which the interaction between the QM charge density and the SEF is approximated using ElectroStatic Potential Fitted (ESPF) multipole operators.[18] Then we apply this ESPF-based QM/MM method to investigate how the magnitude and direction of a SEF impact the electronic structure of retinal in GR[11], along the isomerization pathway in its first singlet excited state.

2 Methods

Finite-field perturbation theory (FFPT) is the standard way for including the effect of a SEF in a quantum chemical calculation. It consists in complementing the one-electron Hamiltonian matrix with proper one-electron integrals of the type $\langle\chi_\mu|\mathbf{r}\cdot\mathbf{F}|\chi_\nu\rangle$ for a given atomic basis set $\{|\chi_\mu\rangle\}$. This approach is available in the OpenMolcas software [19–21], which we use as benchmark throughout the present study to produce reference energies, atomic charge distributions and dipole moments of molecules.

However, since *ab initio* quantum chemistry cannot be applied to molecular systems as large as a rhodopsin protein using a reasonable amount of computer time and resources, we rely on the ESPF-based QM/MM method[18, 22], also implemented in OpenMolcas, whose electrostatic interaction energy ΔE between the QM subsystem and its surroundings (MM and SEF) is:

$$\Delta E = \sum_{a=1}^{N_{QM}} \mathbf{M}_a \cdot \boldsymbol{\phi}(\mathbf{r}_a) - \boldsymbol{\mu}\cdot\mathbf{F} \tag{1}$$

in which the QM density of charges is approximated by point multipoles $\mathbf{M}_a$ centered on each of the N_{QM} QM centers and interacting with the MM electrostatic potential and derivatives $\boldsymbol{\phi}$ at position $\mathbf{r}_a = [x_a, y_a, z_a]$, and complemented with the usual molecular dipole moment $\boldsymbol{\mu}$ interaction with the SEF $\mathbf{F}$ (using the chemistry convention). Higher terms (polarizabilities, hyperpolarizabilities, ...) in the Taylor expansion have not been considered in the present work. While they are required when a perturbative treatment introduces the effect of the electric field (as demonstrated in the case of SEF-dependent activation barriers[23]), the ESPF method features a relaxed electron density, i.e. includes the response of the electronic wavefunction to the SEF, through polarized atomic charge (ESPF0) and dipole (ESPF1) operators. In the ESPF

method, point multipoles $\mathbf{M}_a$ are expectation values of atomic multipole operators, ensuring the polarization of the QM wavefunction by its electrostatic environment. In the following, we truncate the QM multi-centered multipolar expansion to 1st order, i.e. atom-centered charges and dipoles $\mathbf{M}_a = [q_a, \mu_a^x, \mu_a^y, \mu_a^z] = [q_a, \boldsymbol{\mu}_a]$. The second term in Eq.(1), due to the SEF, can be easily approximated using the same ESPF approach:

$$\boldsymbol{\mu} = \sum_{a=1}^{N_{QM}} (q_a \mathbf{r}_a + \boldsymbol{\mu}_a) = \sum_{a=1}^{N_{QM}} \boldsymbol{M}_a \cdot \tilde{\mathbf{r}}_a \tag{2}$$

in which $\tilde{\mathbf{r}}_a$ is a rectangular matrix:

$$\tilde{\mathbf{r}}_a = \begin{pmatrix} x_a & y_a & z_a \\ 1 & 0 & 0 \\ 0 & 1 & 0 \\ 0 & 0 & 1 \end{pmatrix} \tag{3}$$

Combining Eqs. (1) and (2) results in:

$$\begin{aligned} \Delta E &= \sum_{a=1}^{N_{QM}} \mathbf{M}_a \cdot \boldsymbol{\phi}(\mathbf{r}_a) - \left(\sum_{a=1}^{N_{QM}} \mathbf{M}_a \cdot \tilde{\mathbf{r}}_a \right) \cdot \mathbf{F} \\ &= \sum_{a=1}^{N_{QM}} \mathbf{M}_a \cdot (\boldsymbol{\phi}(\mathbf{r}_a) - \tilde{\mathbf{r}}_a \cdot \mathbf{F}) \end{aligned} \tag{4}$$

The term $\boldsymbol{\phi}'(\mathbf{r}_a) = \boldsymbol{\phi}(\mathbf{r}_a) - \tilde{\mathbf{r}}_a \cdot \mathbf{F}$ represents an effective electrostatic potential (and derivatives) at the QM position $\mathbf{r}_a$. The interaction energy between the MM subsystem and the SEF is straightforward and adds a constant term to the total QM/MM energy of a given molecular geometry, eg:

$$\Delta E = \sum_{a=1}^{N_{QM}} \mathbf{M}_a \cdot \boldsymbol{\phi}'(\mathbf{r}_a) - \sum_{i=1}^{N_{MM}} q_i \mathbf{r}_i \cdot \mathbf{F} \tag{5}$$

in the case of a standard non-polarizable MM forcefield, comprising N_{MM} point charges at positions $\mathbf{r}_i$. Accordingly, each Fock matrix element $F_{\mu\nu}$ has to be complemented with the following one-electron contribution:

$$\frac{\partial \Delta E}{\partial P_{\mu\nu}} = \sum_{a=1}^{N_{QM}} \frac{\partial \mathbf{M}_a}{\partial P_{\mu\nu}} \cdot \boldsymbol{\phi}'(\mathbf{r}_a) \tag{6}$$

since only the QM-centered multipoles depend on the electron density matrix elements $P_{\mu\nu}$. This approach is implemented in a development version of OpenMolcas coupled to Tinker version 6.3.3[24].

The analysis of the different potential energy surfaces and/or excitation energies can be made easier thanks to a simple total energy decomposition scheme:

$$E(\mathbf{F}) = E^{\mathrm{QM}}(\mathbf{F}) + E^{\mathrm{MM}} + \Delta E(\mathbf{F}) \tag{7}$$

in which $E^{\mathrm{QM}}(\mathbf{F})$ (resp. E^{MM}) is the SEF-dependent (resp. SEF-independent) energy of the QM (resp. MM) subsystem and $\Delta E(\mathbf{F})$, already introduced in Eq.(5), can be rewritten:

$$\Delta E(\mathbf{F}) = \Delta E^{\mathrm{QM/F}}(\mathbf{F}) + \Delta E^{\mathrm{MM/F}}(\mathbf{F}) + \Delta E^{\mathrm{QM/MM}}(\mathbf{F}) \tag{8}$$

with:

$$\Delta E^{\mathrm{QM/F}}(\mathbf{F}) = -\sum_{a=1}^{N_{QM}} \mathbf{M}_a(\mathbf{F}) \cdot \tilde{\mathbf{r}}_a \cdot \mathbf{F} = -\boldsymbol{\mu}^{\mathrm{QM}}(\mathbf{F}) \cdot \mathbf{F} \tag{9}$$

$$\Delta E^{\mathrm{MM/F}}(\mathbf{F}) = -\sum_{i=1}^{N_{MM}} q_i \mathbf{r}_i \cdot \mathbf{F} = -\boldsymbol{\mu}^{\mathrm{MM}} \cdot \mathbf{F} \tag{10}$$

$$\Delta E^{\mathrm{QM/MM}}(\mathbf{F}) = \sum_{a=1}^{N_{QM}} \mathbf{M}_a(\mathbf{F}) \cdot \boldsymbol{\phi}(\mathbf{r}_a) \tag{11}$$

The second term, Eq.(10), describes the interaction between the MM point charges and the SEF. Accordingly, it behaves linearly with respect to the SEF (for a given molecular structure). This is (formally) not the case for the first term, Eq.(9), which describes the interaction between the QM subsystem and the SEF. Finally, the last term, Eq.(11), describes how the QM/MM interaction energy changes in the presence of the SEF, because of the QM electron density re-polarization by the SEF.

3 Results

3.1 Comparison of FFPT and ESPF

The ESPF method approximates the electrostatic interaction between a quantum distribution of charges and the SEF. We first compare FFPT-based results (relative energies and dipole moments) with the ESPF-based ones, using either ESPF at order 0 (charges only, hereafter denoted ESPF0) and at order 1 (charges and dipoles, hereafter denoted ESPF1). A single water molecule is selected as testbed, using Hartree-Fock theory and the ANO-RCC-VDZP basis set,[25, 26] together with the resolution of identity based on the Cholesky decomposition (RICD) acceleration of the self-consistent field resolution, as available in OpenMolcas.[27] This water molecule experiences a SEF aligned with the $z-$axis, with an intensity ranging from $-1000\,\mathrm{MV\,cm^{-1}}$ to $+1000\,\mathrm{MV\,cm^{-1}}$. Notice that the water dipole moment and the SEF are not parallel (Figure 1A).

In Figure 1B, water total energies (relative to the absence of SEF) confirm that both FFPT and ESPF0/ESPF1 give equivalent results when the SEF intensity is small enough, typically lower than $500\,\mathrm{MV\,cm^{-1}}$. This regime is characterized by a linear

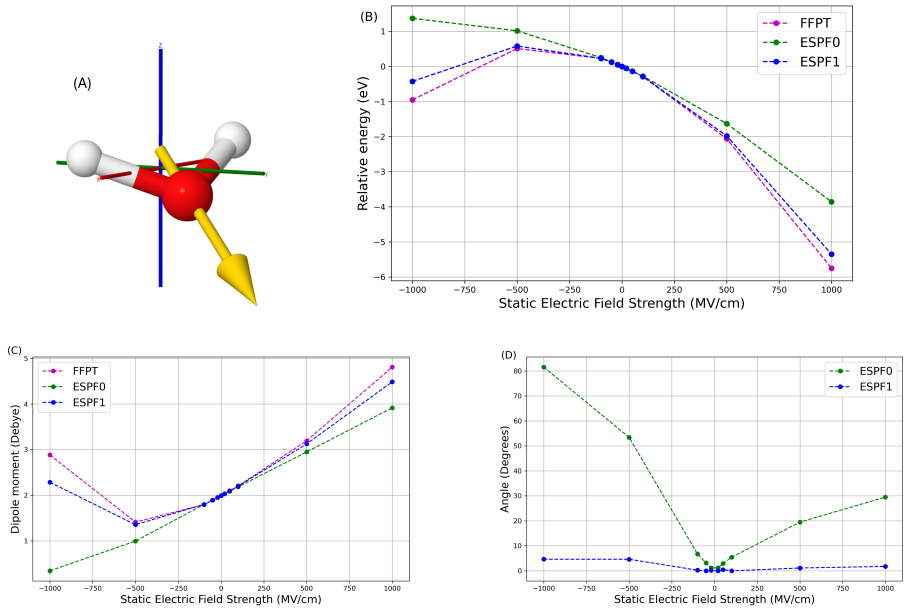

Fig. 1: (A) Orientation of the water molecule in Cartesian space, with its dipole moment as yellow arrow, in the absence of a SEF. When applied, the SEF is collinear to the vertical $z-$axis. (B) Water energy (in eV), relative to the energy in the absence of SEF. (C) Water dipole moment (in Debye). (D) Angle between FFPT and ESPF dipole moments (in °).

coupling between the (qualitatively constant) water dipole moment and the SEF. Their parallel alignment ensures stabilization. However, when the SEF intensity becomes larger than $500\,\mathrm{MV\,cm^{-1}}$, the ESPF0 energies become significantly different from the ESPF1 and FFPT ones, indicating that the 3 ESPF point charges cannot correctly approximate the strong electronic reorganization induced by the intense external field. This behavior is confirmed by inspecting the water dipole moments in Figure 1C. The situation for $-1000\,\mathrm{MV\,cm^{-1}}$ is peculiar: the field is so intense that the water molecule electronic structure is significantly different from the ones computed at other SEF strengths. For instance, the three ESPF atomic charges are -0.01 for oxygen, 0.05 for one hydrogen and -0.04 for the other one, instead of the usual large negative charge at the oxygen center and the complementary positive charges at the hydrogen ones (at $-20\,\mathrm{MV\,cm^{-1}}$: -0.70, 0.36, 0.34). Interestingly, the ESPF1 approximation (ie. point charges and dipoles) is flexible enough to result in energies and molecular dipoles in good agreement with the FFPT benchmark values. The angle between the water dipole moment using FFPT and the one using ESPF confirms this analysis (Figure 1D): it can be as large as 83° with ESPF0, while it always remains lower than 5° with ESPF1. To further validate these findings, we repeated the analysis of the relative energies and dipole moments for N_2, CO_2 and benzene, confirming the ability of the

ESPF1 approximation to reproduce the FFPT results with satisfying accuracy (see Supporting Information).

The results discussed above indicate that ESPF, and especially ESPF1 featuring QM-centered atomic charges and dipoles, represents an efficient alternative to FFPT. Moreover, when the SEF strength remains sufficiently low, which is the case in typical applications for which the effect of the SEF is linear within the energy, ESPF0 can be used safely. As a final note, the dipole moment deriving from equation 2 is barely different from that obtained as the mean value of the position operator (Supporting Information), confirming the effectiveness of the ESPF approximation in most cases.

3.2 Application to a minimal protonated Schiff base

The first application deals with a protonated Schiff base featuring 3 conjugated double bonds (PSB3), a reduced model of the retinal chromophore, ubiquitous in virtually all rhodopsin proteins. Here, we would like to (i) assess the ability of ESPF to reproduce a potential energy surface of PSB3 in its first three singlet states (S_0, S_1, S_2) and (ii) evaluate the effect of a large SEF on PSB3 photoisomerization, assuming the gas phase pathway is not significantly modified by the application of the SEF. In other words, the present work focuses on the electronic structure modifications triggered by the SEF.

Accordingly, we first produce a gas phase minimum energy path (MEP) between the PSB3 Franck-Condon geometry and its S_0/S_1 conical intersection, at the CASSCF/ANO-RCC-VDZP level of theory, with 6 electrons in 6 π orbitals (details are provided as Supporting Information). Once the corresponding potential energy curve is obtained (Figure 2 top center), we recompute the total energies in the presence of a large SEF (about 100 MV cm^{-1}), parallel (Figure 2 top right) or antiparallel (Figure 2 top left) to the PSB3 dipole moment in S_0 (shown as Supporting Information). Once we have assessed the excellent agreement between FFPT- and ESPF-based potential energy surfaces (PES) (provided as Supporting Information), we first observe that the PSB3 thermal isomerization energy decreases in the presence of the SEF, especially when it is parallel to the chromophore dipole moment. Consequently, the application of a SEF would increase the competition between thermal and photoinduced PSB3 isomerization. The application of the SEF lifts the energy degeneracy between S_0 and S_1, while an energy barrier appears in S_1. When the SEF is parallel to the PSB3 dipole moment, the large energy gap between S_1 and S_2 is preserved. The PSB3 dipole moment is also influenced by this SEF. Its value in S_0 and S_2 is becomes much larger than the one in S_1. Moreover, its variations along the isomerization path is dramatically changed, resulting from the state interaction modifications induced by the SEF. In contrast, when the SEF is antiparallel to the PSB3 dipole moment, the S_1 and S_2 potential energy curves become almost degenerate when the isomerization effectively starts. The PSB3 dipole moment is significantly reduced, irrespective of the electronic state (less than 3 Debye).

The influence of the SEF can be further analyzed using the center of the PSB3 +1 electric charge (CoC), see the Supplementary Information for the definition. In the absence of the SEF, the CoC in S_1 moves further away from its initial position while the isomerization proceeds. Conversely, in S_0 and S_2, the CoC comes closer to the N

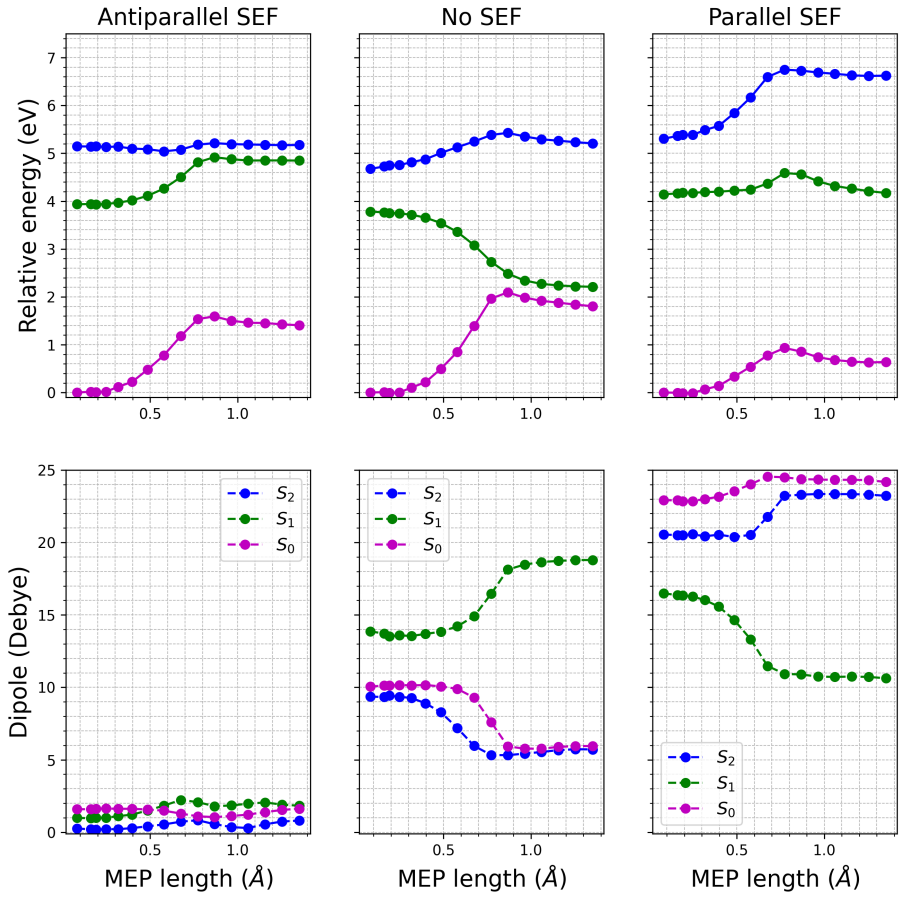

Fig. 2: Top: PSB3 three lowest singlet state energy curves, using the ESPF0 approximation. When ESPF1 is used instead of ESPF0, the resulting plots are virtually identical (see Supporting Information). Bottom: corresponding PSB3 dipole moments. The orientation of the (anti-)parallel electric field with respect to retinal is the same as for water in Fig. 1A.

center (Figure 3 center). When the SEF is antiparallel to the PSB3 dipole moment (Figure 3 left), the intensity of the field is large enough to maintain the CoC at the N center, even during the PSB3 isomerization. In other words, the antiparallel SEF blocks the well-known PSB3 (and retinal) charge translocation upon excitation from S_0 to S_1, it prevents the PSB3 photoisomerization and ultimately the photoexcited PSB3 would emit light without any Stokes shift (Figure 2 left). We shall nevertheless

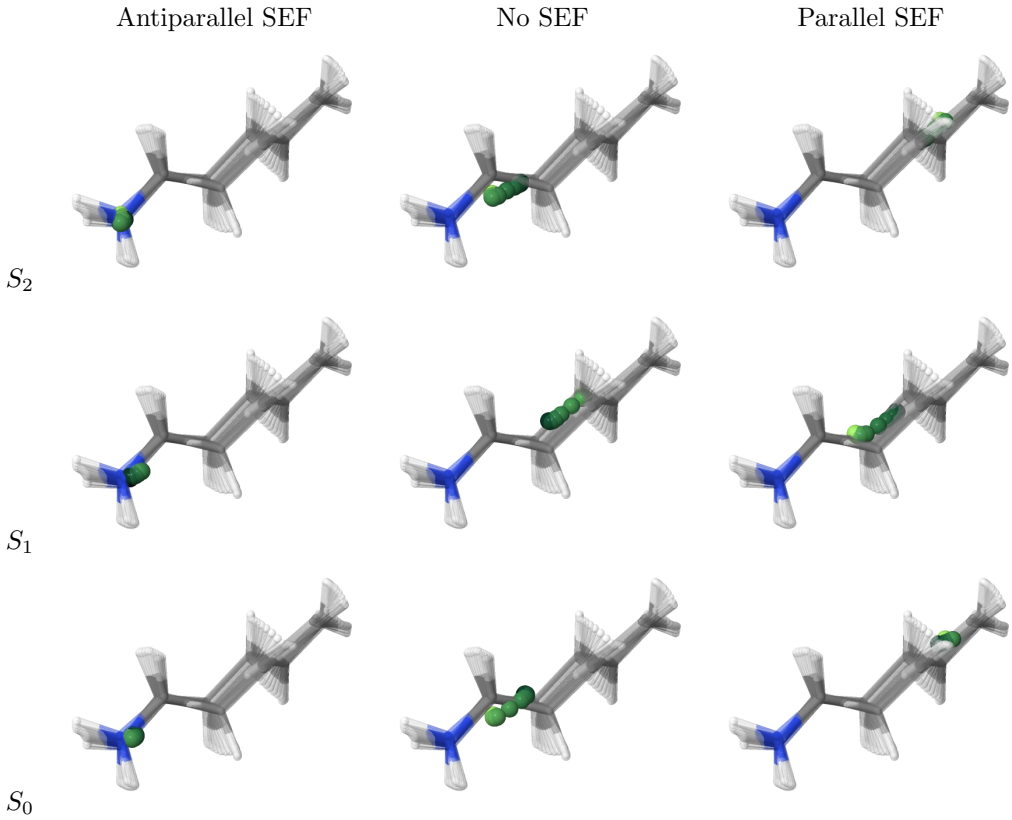

Fig. 3: Superposition of PSB3 structures along the S_1 isomerization MEP. PSB3 center of charge is shown as a dark green to light green sphere.

notice that the $S_0 \rightarrow S_1$ oscillator strength never exceeds 0.015, resulting in a very low light absorption probability.

More interestingly, when the SEF is parallel to the PSB3 dipole moment (Figure 3 right), the initial location of the CoC is further away from the nitrogen center (with respect to its position in the absence of SEF), and remains almost unchanged in S_0 and S_2 as the PSB3 isomerization proceeds. On the other hand, in S_1 the CoC flows back toward the nitrogen center, especially when the BLA coordinate is active. Consequently, the charge transfer character of S_1 increases with the PSB3 twisting progress. Nevertheless, the presence of the 0.4 eV barrier in S_1 would probably prevent the PSB3 to photoisomerize, like in the anti-parallel case.

3.3 Application to Gloeobacter rhodopsin

The PSB3 results above, together with Garavelli's and coworkers' results[14], suggest that sufficiently large SEF, ie. larger than 10 MV cm^{-1} may dramatically modify the retinal photochemistry. Hereafter, we would like to assess how a smaller SEF of

5 MV cm^{-1} competes with the opsin local electric field, using the microbial Gloeobacter rhodopsin (GR) as testbed.[28] This field strength is meant to approximately represent how the transmembrane charge imbalance could by modified by a local modification of the ion concentrations.

The GR model structure (Figure 4 left) has been obtained using PDB id 6NWD [29] as initial structure in the Automatic Rhodopsin Model (ARM) protocol[30, 31], selecting the following manual parameter settings[32]: the pH is set to 7.5; all histidines are deprotonated, except H87; the retinal counterions, D121 and D253, are kept deprotonated. Geometry optimization of the retinal chromophore and the cavity amino-acid

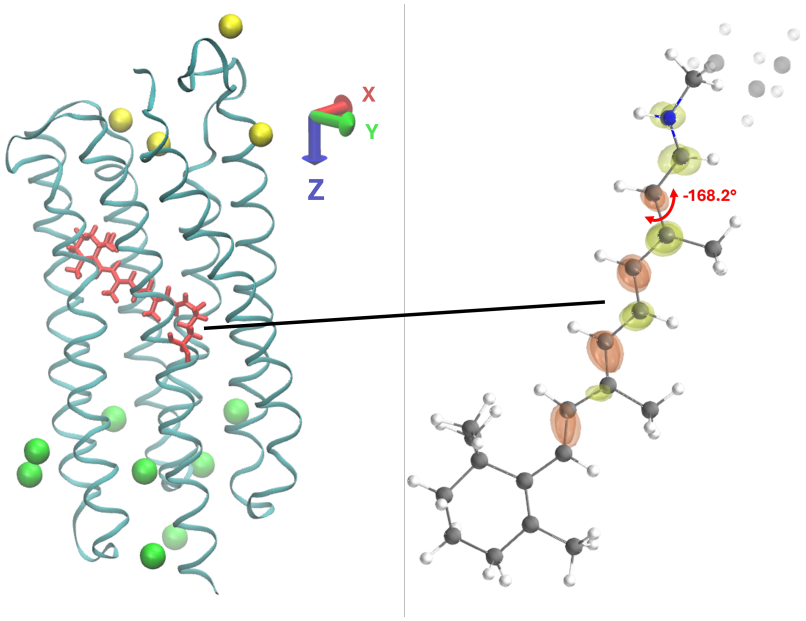

Fig. 4: Left: GR structure, with cartesian axes (the SEF is applied along the z axis) and with explicit positions of retinal (red sticks), sodium cations (green balls) and chloride anions (yellow balls). Right: S_0 QM/MM optimized retinal geometry, showing the electron density difference between S_0 and S_1 states and the C12=C13 torsion angle.

side-chains is performed at the XMS-CASPT2/6-31G*/Amber94 level of theory, in the absence of any SEF. The active space comprises 12 electrons in 12 π orbitals. Using this single structure, the influence of SEF with various strengths and directions is assessed with XMS-CASPT2/6-31G*/Amber single point calculations, including up to 5 singlet states. In the following, we consider the case of the SEF direction perpendicular to the membrane mean plane (z axis, the default orientation provided by the ARM protocol), keeping all the structural parameters unchanged (Figure 4).

In Figure 5, we report three different metrics of the $S_0 \rightarrow S_1$ and $S_0 \rightarrow S_2$ transitions: XMS-CASPT2 vertical excitation energy, transition dipole and location of the

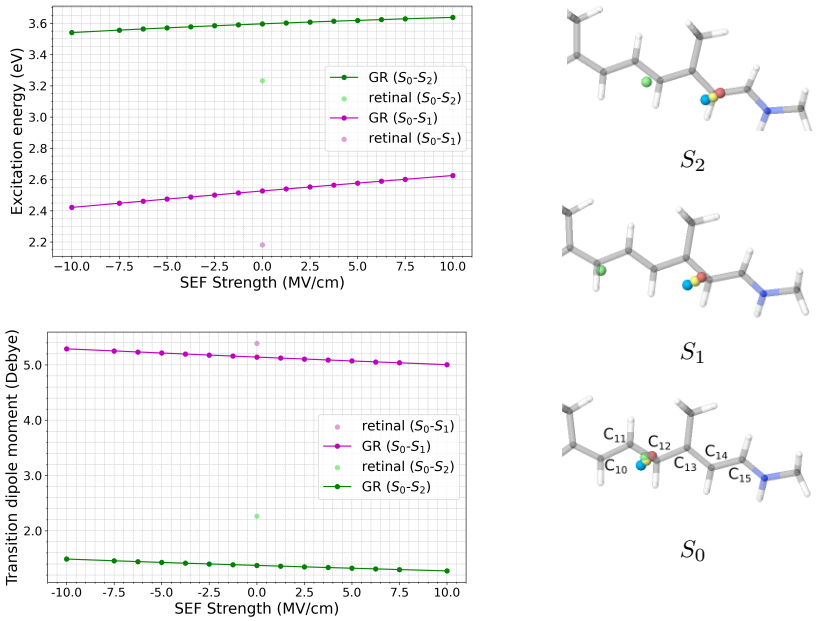

Fig. 5: Top left: Excitation energies of GR and retinal, bottom left: transition dipole moments of GR and retinal, both respective to SEF in z-direction (transmembrane). Right: CoC position of bare retinal CoC (green), GR retinal without SEF (yellow), GR retinal with SEF (red: 10.0 MV cm^{-1}, blue: -10.0 MV cm^{-1}). Only the C9-N part of retinal is shown, for the sake of good visualization.

retinal center of (+1) charge. In agreement with the abundant literature,[33–35], we find that the electrostatic effect of the GR opsin increases the $S_0 \rightarrow S_1$ and $S_0 \rightarrow S_2$ excitation energies. This blue shift is mainly associated to the retinal counterion negative charge, located at a short distance from the retinal PSB positive charge, stabilizing the retinal ground state S_0 more than the other electronic states (in which the charge is translocated towards the retinal β-ionone ring). Transition dipoles are reduced, slightly in the case of $S_0 \rightarrow S_1$, while more dramatically for $S_0 \rightarrow S_2$. This result can be rationalized by the inspection of the location of the retinal center of (+1) charge (CoC). In bare retinal, the CoC is located close to the C12 carbon atom in S_0 and in S_2, while it is translocated towards the β-ionone ring in S_1, close to the C10 carbon atom. The introduction of the MM electrostatic potential impacts the CoC location in two different ways: in S_0 it barely changes its location (C12), while it moves towards the protonated Schiff base (C14) in S_1 and S_2.

Switching on the SEF, either parallel (positive) or antiparallel (negative) to the retinal S_0 dipole moment z component, the QM/MM excitation energies are modified. The application of a parallel (resp. antiparallel) SEF results in linearly increasing (resp. decreasing) excitation energies, with a rate about 0.010 eV / (MV cm^{-1}) in the case of $S_0 \rightarrow S_1$, twice larger that it is for $S_0 \rightarrow S_2$. This trend can be easily explained, since

the GR total energy responds linearly to the SEF and proportionally to the retinal dipole moment in each electronic state (reported as Supplementary Information). As a matter of fact, the retinal dipole moment is smaller in S_1 compared to S_0 or S_2. In agreement with the variation of the excitation energies with the SEF, the two transition dipole moments linearly decrease (resp. increase) when the applied SEF is parallel (resp. antiparallel). Their respective slopes are similar, about -0.01 D (MV cm^{-1}). Nevertheless, the character of each transition remains unaffected by the application of the SEF, because of its low intensity, as evidenced by the CoC positions which are only displaced a few tenth of Å when the SEF is applied.

These findings can be rationalized by analyzing the competition between the MM electric field and the SEF (Figure 6). The MM distribution of point charges generates

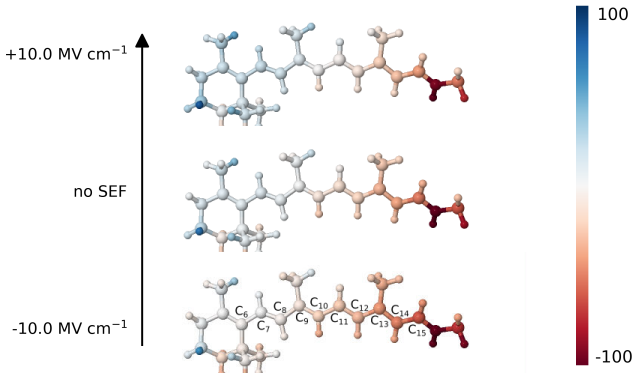

Fig. 6: Intensity of the total electric field in the z-direction, due to the MM charge distribution and to the SEF in three cases: $-10.0\,\mathrm{MV\,cm^{-1}}$ (left), no SEF (middle) and $10.0\,\mathrm{MV\,cm^{-1}}$ (right). For the sake of clarity, values larger than $\pm 100\,\mathrm{MV\,cm^{-1}}$ are shown with this maximum value.

the largest (positive) electric field in the PSB region of retinal. Consequently, the application of the SEF only marginally modifies the total electric field in part of the chromophore. However, this is not the case in the C6 to C12 region, where the total electric field is indeed modulated by the SEF, in intensity (eg. C12) or even in direction (eg. C8). Accordingly, in that part of retinal, the application of a SEF, even moderate, locally modifies its electronic structure, as seen in the CoC displacement (Figure 5).

Taking advantage of the energy decomposition scheme presented in section 2, Eqs. 8 to 11, we can analyze how the application of the SEF modifies the interaction energies, in each electronic state. Starting with S_0 (Figure 7, left panel), the total interaction energy stabilizes (destabilizes) the GR system when the SEF is parallel (antiparallel) to the z direction. This trend is mainly due to the repolarization of the QM electronic structure, as evidenced by the largest slope of the almost linear $\Delta E^{QM/F}$ term, even if the linear $\Delta E^{MM/F}$ slope shows the opposite trend. Notice that the QM/MM interaction energy is barely modified by the repolarization of the QM subsystem. Considered together, these results confirm that the application of the

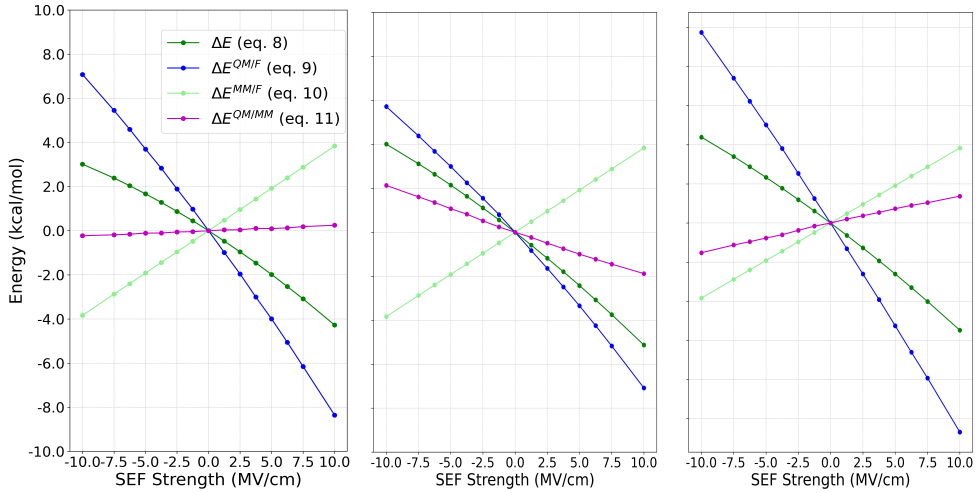

(a) S_0 (b) S_1 (c) S_2

Fig. 7: Interaction energy decomposition for (a) S_0, (b) S_1 and (c) S_2 as a function of the SEF. The reference energy corresponds to the QM/MM interaction energy with static electric field. The definitions of the total interaction scheme and its decomposed terms can be found in eq. 8 to 11.

SEF with such a limited intensity can be modeled by a quasi-constant (QM+MM) dipole / SEF single interaction term.

Qualitatively, this analysis remains valid for S_1 and S_2 (Figure 7 middle and right panels). We note that the $\Delta E^{QM/F}$ term shows a more pronounced curvature in S_0 and S_1 than in S_2 when the SEF varies. Accordingly, the retinal dipole moment varies more rapidly in the former states, suggesting the corresponding retinal electronic structures to be more polarizable by the application of the SEF. The $\Delta E^{QM/MM}$ variation is much larger in S_1 and S_2 than in S_0. Moreover, their slopes show different signs. Accordingly, the retinal-opsin interaction is stabilized in S_1 when the SEF increases, whereas it is destabilized in S_2, eventually tuning their energy gaps and possibly the associated retinal photodynamics.

In order to get a deeper insight of the SEF effect on the retinal photochemistry in GR, we study its effect on an approximated retinal photoisomerization potential energy surface (PES), ie. fixing the C12-C13=C14-C15 torsion angle (from $-170°$ to $-90°$) while optimizing the other degrees of freedom at the XMS-CASPT2/6-31G(d)/Amber level of theory, determined in the absence of the SEF. In Figure 8 left panel, we report such a PES, as well as its modification when a $\pm 5\,\mathrm{MV\,cm^{-1}}$ SEF is applied. This choice of SEF strength is inspired by a recent article [28] in which the application to bacteriorhodopsin (BR) of an ultrafast $3\,\mathrm{MV\,cm^{-1}}$ terahertz pulse induces a retinal light absorption change, eventually revealing a more important change of the retinal dipole moment in S_2 rather than in S_1, interpreted as the signature of an important mixing between the two BR excited states. In Figure 8 right panel, we also report

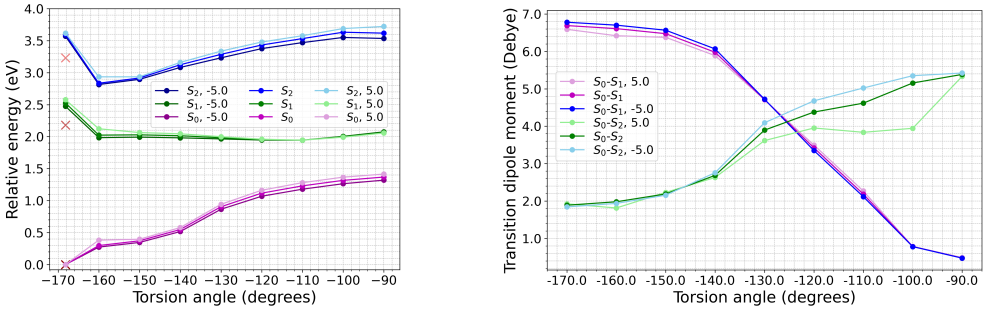

Fig. 8: Left: Approximate retinal isomerization potential energy pathways in S_1, in the absence or in the presence of a SEF. The S_0 minimum energy is set to 0.0 eV as reference. Retinal energies for S_0, S_1, S_2 are depicted with crosses for comparison. Right: $S_{\rightarrow}S_1$ and $S_{\rightarrow}S_2$ transition dipole moments along the same pathway.

the $S_0 \rightarrow S_1$ and $S_0 \rightarrow S_2$ transition dipole moments as a way to highlight the SEF-induced electronic structure modifications as the retinal isomerization proceeds.

In the absence of SEF, QM/MM interactions blue-shift the retinal excited states, as already reported in Figure 5. Then, proceeding along the retinal isomerization approximate coordinate, S_0 and S_1 come closer to each other, while the gap with S_2 increases. A potential energy minimum is found in S_1, between $-120°$ and $-110°$. Even at torsion angle close to $-90°$, the energy gap between S_0 and S_1 remains large, ie. the retinal structures remain quite far away from the expected conical intersection region in which excited GR can efficiently decay to its ground state. The applied weak SEF barely modifies the energy curves. However, this apparently weak SEF effect becomes more important when one looks at the state electronic structure, or equivalently, at the transition dipoles (Figure 8 right panel). On one hand, the SEF does not modify the $S_0 \rightarrow S_1$ transition dipole (which decreases when the isomerization proceeds), whether it is applied parallel or anti-parallel to the z axis. On the other hand, the $S_0 \rightarrow S_2$ transition dipole (which increases when the isomerization proceeds) shows significant variations when the torsion angle becomes lower than $-140°$. Taken together, these results suggest that the application of the SEF, even with a low intensity, may modify the couplings between GR S_2 and higher excited states.

4 Conclusion

An extension of the ESPF QM/MM method has been introduced, allowing to take into account the electrostatic interaction between a QM/MM model of a (macro-)molecule together with its molecular environment and an external static electric field. Thanks to the ESPF approach in which the QM charge distribution is represented as a multipolar multicenter expansion, the total interaction energy can be easily decomposed as a sum of three contributions - QM dipole/SEF, MM dipole/SEF and QM/MM - eventually allowing for a deeper analysis of the electric field effect.

Having validated the method and tested its accuracy with respect to the SEF intensity, we applied the method to the isomerization reaction of PSB3 in its first singlet excited state, demonstrating how large electric fields can profoundly modify potential energy surfaces. PSB3 being a cation, we have illustrated the effect of the SEF with the displacement of the molecule +1 center of charge.

We finally studied the competition between a weak SEF and the local electric field due to a protein amino-acid and ions charge distribution. In particular, our results suggest that the SEF, even with a low strength, may induce noticeable changes in the retinal electronic wavefunctions, even if the isomerization pathway of retinal in GR is barely modified.

In the near future, the method will be developed further. The implementation of energy gradients will allow us to perform geometry optimizations and to carry on (non-adiabatic) molecular dynamics, opening new possibilities to investigate how GR (and other rhodopsin proteins) photodynamics are modified by the application of a static or oscillating electric field.

Supplementary information. Inputs for OpenMolcas/Tinker calculations, in the case of water, and PSB3; comparision between FFPT, ESPF0 and ESPF1 for N_2, CO_2, benzene; comparison between FFPT and ESPF state energies along the PSB3 MEP; OpenMolcas/Tinker inputs for GR XMS-CASPT2 singles points and geometry optimizations; link to the GR geometries; computation of CoC; GR state energies.

Declarations

No funding was received for conducting this study.

Authors' Contribution statement using CRediT: Isabel Eder: Data Curation, Formal Analysis, Investigation, Validation, Writing. Miquel Huix-Rotllant: Conceptualization, Methodology, Software, Supervision (equal), Writing. Nicolas Ferré; Conceptualization, Data Curation, Formal Analysis, Investigation, Methodology, Project Administration, Resources, Software, Supervision (equal), Validation, Visualization, Writing.

References

[1] Bezanilla, F.: How membrane proteins sense voltage. Nat. Rev. Mol. Cell Bio. **9**(4), 323–332 (2008) https://doi.org/10.1038/nrm2376

[2] Calisto, F., Sousa, F.M., Sena, F.V., Refojo, P.N., Pereira, M.M.: Mechanisms of energy transduction by charge translocating membrane proteins. Chem. Rev. **121**(3), 1804–1844 (2021) https://doi.org/10.1021/acs.chemrev.0c00830

[3] Clair, E.C.S., Ogren, J.I., Mamaev, S., Kralj, J.M., Rothschild, K.J.: Conformational changes in the archaerhodopsin-3 proton pump: detection of conserved strongly hydrogen bonded water networks. J. Biol. Phys. **38**(1), 153–168 (2012) https://doi.org/10.1007/s10867-011-9246-4

[4] Maclaurin, D., Venkatachalam, V., Lee, H., Cohen, A.E.: Mechanism of voltage-sensitive fluorescence in a microbial rhodopsin. Proc. Natl. Acad. Sci. **110**(15), 5939–5944 (2013) https://doi.org/10.1073/pnas.1215595110

[5] Vlasova, A.D., Bukhalovich, S.M., Bagaeva, D.F., Polyakova, A.P., Ilyinsky, N.S., Nesterov, S.V., Tsybrov, F.M., Bogorodskiy, A.O., Zinovev, E.V., Mikhailov, A.E., Vlasov, A.V., Kuklin, A.I., Borshchevskiy, V.I., Bamberg, E., Uversky, V.N., Gordeliy, V.I.: Intracellular microbial rhodopsin-based optogenetics to control metabolism and cell signaling. Chem. Soc. Rev. **53**(7), 3327–3349 (2024) https://doi.org/10.1039/d3cs00699a

[6] Skopintsev, P., Ehrenberg, D., Weinert, T., James, D., Kar, R.K., Johnson, P.J.M., Ozerov, D., Furrer, A., Martiel, I., Dworkowski, F., Nass, K., Knopp, G., Cirelli, C., Arrell, C., Gashi, D., Mous, S., Wranik, M., Gruhl, T., Kekilli, D., Brünle, S., Deupi, X., Schertler, G.F.X., Benoit, R.M., Panneels, V., Nogly, P., Schapiro, I., Milne, C., Heberle, J., Standfuss, J.: Femtosecond-to-millisecond structural changes in a light-driven sodium pump. Nature (2020) https://doi.org/10.1038/s41586-020-2307-8

[7] Delemotte, L., Tarek, M.: Molecular dynamics simulations of lipid membrane electroporation. J. Membr. Biol. **245**(9), 531–543 (2012) https://doi.org/10.1007/s00232-012-9434-6

[8] Roux, B.: The membrane potential and its representation by a constant electric field in computer simulations. Biophys. J. **95**(9), 4205–4216 (2008) https://doi.org/10.1529/biophysj.108.136499

[9] Melcr, J., Bonhenry, D., Timr, S., Jungwirth, P.: Transmembrane potential modeling: Comparison between methods of constant electric field and ion imbalance. J. Chem. Theory Comput. **12**(5), 2418–2425 (2016) https://doi.org/10.1021/acs.jctc.5b01202

[10] Kasparyan, G., Hub, J.S.: Equivalence of charge imbalance and external electric fields during free energy calculations of membrane electroporation. J. Chem. Theory Comput. **19**(9), 2676–2683 (2023) https://doi.org/10.1021/acs.jctc.3c00065

[11] Choi, A.R., Shi, L., Brown, L.S., Jung, K.-H.: Cyanobacterial Light-Driven Proton Pump, Gloeobacter Rhodopsin: Complementarity between Rhodopsin-Based Energy Production and Photosynthesis. PLOS ONE **9**(10), 110643 (2014) https://doi.org/10.1371/journal.pone.0110643

[12] Engqvist, M.K.M., McIsaac, R.S., Dollinger, P., Flytzanis, N.C., Abrams, M., Schor, S., Arnold, F.H.: Directed evolution of gloeobacter violaceus rhodopsin spectral properties. J. Mol. Biol. **427**(1), 205–220 (2015) https://doi.org/10.1016/j.jmb.2014.06.015

[13] Tutol, J.N., Lee, J., Chi, H., Faizuddin, F.N., Abeyrathna, S.S., Zhou, Q., Morcos,

F., Meloni, G., Dodani, S.C.: A single point mutation converts a proton-pumping rhodopsin into a red-shifted, turn-on fluorescent sensor for chloride. Chem. Sci. **12**(15), 5655–5663 (2021) https://doi.org/10.1039/d0sc06061e

[14] El-Tahawy, M.M.T., Nenov, A., Garavelli, M.: Photoelectrochromism in the Retinal Protonated Schiff Base Chromophore: Photoisomerization Speed and Selectivity under a Homogeneous Electric Field at Different Operational Regimes. J. Chem. Theory Comput. **12**(9), 4460–4475 (2016) https://doi.org/10.1021/acs.jctc.6b00558

[15] Senn, H.M., Thiel, W.: QM/MM Methods for Biolomolecular Systems. Angew. Chem. Int. Ed. **48**(7), 1198–1229 (2009) https://doi.org/10.1002/anie.200802019

[16] Ho, J., Yu, H., Shao, Y., Taylor, M., Chen, J.: How accurate are qm/mm models? J. Phys. Chem. A **129**(6), 1517–1528 (2024) https://doi.org/10.1021/acs.jpca.4c06521

[17] Huix-Rotllant, M., Ferré, N.: Analytic energy, gradient, and hessian of electrostatic embedding qm/mm based on electrostatic potential-fitted atomic charges scaling linearly with the mm subsystem size. J. Chem. Theory and Comp. **17**(1), 538–548 (2020) https://doi.org/10.1021/acs.jctc.0c01075

[18] Ferré, N., Ángyán, J.G.: Approximate electrostatic interaction operator for QM/MM calculations. Chem. Phys. Lett. **356**, 331–339 (2002) https://doi.org/10.1016/S0009-2614(02)00343-3

[19] Galván, I.F., Vacher, M., Alavi, A., Angeli, C., Aquilante, F., Autschbach, J., Bao, J.J., Bokarev, S.I., Bogdanov, N.A., Carlson, R.K., Chibotaru, L.F., Creutzberg, J., Dattani, N., Delcey, M.G., Dong, S.S., Dreuw, A., Freitag, L., Frutos, L.M., Gagliardi, L., Gendron, F., Giussani, A., González, L., Grell, G., Guo, M., Hoyer, C.E., Johansson, M., Keller, S., Knecht, S., Kovačević, G., Källman, E., Manni, G.L., Lundberg, M., Ma, Y., Mai, S., Malhado, J.P., Malmqvist, P.Å., Marquetand, P., Mewes, S.A., Norell, J., Olivucci, M., Oppel, M., Phung, Q.M., Pierloot, K., Plasser, F., Reiher, M., Sand, A.M., Schapiro, I., Sharma, P., Stein, C.J., Sørensen, L.K., Truhlar, D.G., Ugandi, M., Ungur, L., Valentini, A., Vancoillie, S., Veryazov, V., Weser, O., Wesołowski, T.A., Widmark, P.-O., Wouters, S., Zech, A., Zobel, J.P., Lindh, R.: OpenMolcas: From Source Code to Insight. J. Chem. Theory Comput. **15**(11), 5925–5964 (2019) https://doi.org/10.1021/acs.jctc.9b00532

[20] Aquilante, F., Autschbach, J., Baiardi, A., Battaglia, S., Borin, V.A., Chibotaru, L.F., Conti, I., Vico, L.D., Delcey, M., Galván, I.F., Ferré, N., Freitag, L., Garavelli, M., Gong, X., Knecht, S., Larsson, E.D., Lindh, R., Lundberg, M., Malmqvist, P.Å., Nenov, A., Norell, J., Odelius, M., Olivucci, M., Pedersen, T.B., Pedraza-González, L., Phung, Q.M., Pierloot, K., Reiher, M., Schapiro, I., Segarra-Martí, J., Segatta, F., Seijo, L., Sen, S., Sergentu, D.-C., Stein, C.J., Ungur, L., Vacher, M., Valentini, A., Veryazov, V.: Modern quantum chemistry

with [Open]Molcas. J. Chem. Phys. **152**(21), 214117 (2020) https://doi.org/10.1063/5.0004835

[21] Li Manni, G., Fdez. Galván, I., Alavi, A., Aleotti, F., Aquilante, F., Autschbach, J., Avagliano, D., Baiardi, A., Bao, J.J., Battaglia, S., Birnoschi, L., Blanco-González, A., Bokarev, S.I., Broer, R., Cacciari, R., Calio, P.B., Carlson, R.K., Carvalho Couto, R., Cerdán, L., Chibotaru, L.F., Chilton, N.F., Church, J.R., Conti, I., Coriani, S., Cuéllar-Zuquin, J., Daoud, R.E., Dattani, N., Decleva, P., Graaf, C., Delcey, M.G., De Vico, L., Dobrautz, W., Dong, S.S., Feng, R., Ferré, N., Filatov(Gulak), M., Gagliardi, L., Garavelli, M., González, L., Guan, Y., Guo, M., Hennefarth, M.R., Hermes, M.R., Hoyer, C.E., Huix-Rotllant, M., Jaiswal, V.K., Kaiser, A., Kaliakin, D.S., Khamesian, M., King, D.S., Kochetov, V., Krośnicki, M., Kumaar, A.A., Larsson, E.D., Lehtola, S., Lepetit, M.-B., Lischka, H., López Ríos, P., Lundberg, M., Ma, D., Mai, S., Marquetand, P., Merritt, I.C.D., Montorsi, F., Mörchen, M., Nenov, A., Nguyen, V.H.A., Nishimoto, Y., Oakley, M.S., Olivucci, M., Oppel, M., Padula, D., Pandharkar, R., Phung, Q.M., Plasser, F., Raggi, G., Rebolini, E., Reiher, M., Rivalta, I., Roca-Sanjuán, D., Romig, T., Safari, A.A., Sánchez-Mansilla, A., Sand, A.M., Schapiro, I., Scott, T.R., Segarra-Martí, J., Segatta, F., Sergentu, D.-C., Sharma, P., Shepard, R., Shu, Y., Staab, J.K., Straatsma, T.P., Sørensen, L.K., Tenorio, B.N.C., Truhlar, D.G., Ungur, L., Vacher, M., Veryazov, V., Voß, T.A., Weser, O., Wu, D., Yang, X., Yarkony, D., Zhou, C., Zobel, J.P., Lindh, R.: The OpenMolcas Web: A Community-Driven Approach to Advancing Computational Chemistry. J. Chem. Theory Comput. **19**(20), 6933–6991 (2023) https://doi.org/10.1021/acs.jctc.3c00182

[22] Melaccio, F., Olivucci, M., Lindh, R., Ferré, N.: Unique QM/MM potential energy surface exploration using microiterations. Int. J. Quantum Chem. **111**(13), 3339–3346 (2011) https://doi.org/10.1002/qua.23067

[23] Besalú-Sala, P., Solà, M., Luis, J.M., Torrent-Sucarrat, M.: Fast and simple evaluation of the catalysis and selectivity induced by external electric fields. ACS Catalysis **11**(23), 14467–14479 (2021) https://doi.org/10.1021/acscatal.1c04247

[24] Rackers, J.A., Wang, Z., Lu, C., Laury, M.L., Lagardère, L., Schnieders, M.J., Piquemal, J.-P., Ren, P., Ponder, J.W.: Tinker 8: Software Tools for Molecular Design. J. Chem. Theory Comput. **14**(10), 5273–5289 (2018) https://doi.org/10.1021/acs.jctc.8b00529

[25] Widmark, P.-O., Malmqvist, P.-A., Roos, B.O.: Density matrix averaged atomic natural orbital (ano) basis sets for correlated molecular wave functions. i. first row atoms. Theor. Chim. Acta **77**, 291–306 (1990) https://doi.org/10.1007/bf01120130

[26] Roos, B.O., Lindh, R., Malmqvist, P.-A., Veryazov, V., Widmark, P.-O.: Main group atoms and dimers studied with a new relativistic ano basis set. J. Phys.

Chem. A **108**, 2851–2858 (2004) https://doi.org/10.1021/jp031064+

[27] Aquilante, F., Lindh, R., Pedersen, T.B.: Unbiased auxiliary basis sets for accurate two-electron integral approximations. J. Chem. Phys. **127**(11), 114107 (2007) https://doi.org/10.1063/1.2777146

[28] Zhang, J., Singh, P., Engel, D., Fingerhut, B.P., Broser, M., Hegemann, P., Elsaesser, T.: Ultrafast terahertz stark spectroscopy reveals the excited-state dipole moments of retinal in bacteriorhodopsin. Proc. Natl. Acad. Sci. U. S. A. **121**(26), 2319676121 (2024) https://doi.org/10.1073/pnas.2319676121

[29] Morizumi, T., Ou, W.-L., Van Eps, N., Inoue, K., Kandori, H., Brown, L.S., Ernst, O.P.: X-ray Crystallographic Structure and Oligomerization of Gloeobacter Rhodopsin. Sci. Rep. **9**(1), 11283 (2019) https://doi.org/10.1038/s41598-019-47445-5

[30] Pedraza-González, L., Barneschi, L., Padula, D., De Vico, L., Olivucci, M.: Evolution of the Automatic Rhodopsin Modeling (ARM) Protocol. Top. Curr. Chem. **380**(3), 21 (2022) https://doi.org/10.1007/s41061-022-00374-w

[31] Pedraza-González, L., Barneschi, L., Marszałek, M., Padula, D., De Vico, L., Olivucci, M.: Automated QM/MM Screening of Rhodopsin Variants with Enhanced Fluorescence. J. Chem. Theory Comput. **19**(1), 293–310 (2023) https://doi.org/10.1021/acs.jctc.2c00928

[32] Barreiro-Lage, D., Ledentu, V., D'Ascenzi, J., Huix-Rotllant, M., Ferré, N.: Investigating the Origin of Automatic Rhodopsin Modeling Outliers Using the Microbial Gloeobacter Rhodopsin as Testbed. J. Phys. Chem. B **128**(50), 12368–12378 (2024) https://doi.org/10.1021/acs.jpcb.4c05962

[33] Ernst, O.P., Lodowski, D.T., Elstner, M., Hegemann, P., Brown, L.S., Kandori, H.: Microbial and animal rhodopsins: structures, functions, and molecular mechanisms. Chem. Rev. **114**(1), 126–163 (2014) https://doi.org/10.1021/cr4003769

[34] Luk, H.L., Melaccio, F., Rinaldi, S., Gozem, S., Olivucci, M.: Molecular bases for the selection of the chromophore of animal rhodopsins. Proc. Natl. Acad. Sci. U. S. A. **112**(50), 15297–15302 (2015) https://doi.org/10.1073/pnas.1510262112

[35] Palombo, R., Barneschi, L., Pedraza-González, L., Padula, D., Schapiro, I., Olivucci, M.: Retinal chromophore charge delocalization and confinement explain the extreme photophysics of neorhodopsin. Nat. Commun. **13**(1), 6652 (2022) https://doi.org/10.1038/s41467-022-33953-y